Journal of the Meteorological Society of Japan

EARLY ONLINE RELEASE

The DOI for this manuscript is
DOI:10.2151/jmsj.2021-075
J-STAGE Advance published date: September 6th, 2021
The final manuscript after publication will replace the preliminary version at the above DOI once it is available.

Uncertainties in radiation measurement using a rotating shadow-band spectro-radiometer

Tamio TAKAMURA[1]

Center for Environmental Remote Sensing
Chiba University, Chiba, Japan

and

Pradeep KHATRI

Center for Atmospheric and Oceanic Studies
Tohoku University, Sendai, Japan

February 1, 2021

1) Corresponding author: Tamio Takamura, Center for Environmental Remote Sensing, Chiba University, 1-33, Yayoicho, Inage-ku, Chiba 263-8522 JAPAN
Email:takamura@faculty.chiba-u.jp
Fax: +81-43-290-3857

Abstract

A rotating shadow-band spectro-radiometer system is a powerful tool for surveying light in the environment. It can provide the following spectral components of the solar irradiance without using any traditional solar tracking tool: direct normal irradiance (spDNI), diffuse horizontal irradiance (spDHI), and global horizontal irradiance (spGHI). Both irradiances, spDNI and spDHI, are derived from the combination of spGHI observations at different shadow-band positions. The shadow-band system induces basic errors caused by the imperfect corrections of the diffuse irradiance shadowed by band. To restrict the basic errors to within 2%, the band slant-angle should be within 72 deg for a usual operating condition of the MS-700 spectro-radiometer manufactured by EKO Instruments Co., Ltd. with the MB-20 shadow-band system for MS-700. The errors in the spDNI and spDHI estimation are evaluated quantitatively by using realistic models that consider instrumental and atmospheric conditions. Estimates of spDNI can result in optical depth errors. The relative error in this estimation is described by using a correction coefficient C_{fwd} defined by the ratio of the true diffuse irradiance simulated by the shadowed irradiance to the approximate value observed. The value of C_{fwd} depends on the magnitude of the aerosol optical depth as well as the aerosol type. This error analysis should help to improve the accuracy of this system of measurements.

Key words rotating shadow-band radiometer; error estimation of aerosol optical depth; radiation measurement

1. Introduction

Particles suspended in the atmosphere have two major effects on the modification of the weather and climate through changes in the received solar radiation and cloud formation, known as direct and indirect effects. In recent decades, both effects have been investigated, with focus on climate change issues (e.g., Kim et al. 2005; Nakajima et al. 2007; Bi et al. 2014). The direct effect of aerosols on the climate is relatively straightforward to assess. It can be evaluated if the aerosol optical characteristics are known (i.e., aerosol optical depth (AOD), single scattering albedo (SSA), and asymmetry factor (ASY)). While the radiative transfer mechanism in the atmosphere on how to use such information is known, the distribution of the optical characteristics at the global scale pose a challenge since the aerosols come from different sources and have different chemical compositions.

As described in the IPCC (2014), the uncertainties of the aerosol effects are larger than those of the global greenhouse gases. The biggest part in these uncertainties is due to the lack of knowledge on cloud formation and related mechanisms. Global information on aerosol properties is another issue because these properties are fundamental for both effects. Satellite programs are the most effective for obtaining large scale information. MODIS (Moderate-Resolution Imaging Spectroradiometer) sensors onboard Terra and Aqua (https://terra.nasa.gov/about; https://aqua.nasa.gov; https://modis-images.gsfc.nasa.gov/MOD04_L2/doi.html), developed by NASA (National Aeronautics and Space Administration) have produced substantial information on aerosols and clouds. Recently, geostationary satellites such as Himawari-8/9, launched and operated by JAXA (Japan Aerospace Exploration Agency) and JMA (Japan Meteorological Agency), started to produce aerosol and cloud information using improved sensors and algorithms. The P-Tree System operated by JAXA can supply the quasi-real time information of aerosol and cloud as well as other products, such as short wave radiation, chlorophyll-a and so on (https://www.eorc.jaxa.jp/ptree). These products cover large geographical regions with homogeneous quality, and can provide information on diurnal variability. Such information can extend what is known from missions such as the A-train configuration (Stephens et al. 2018).

The scientific reliability/accuracy of satellite products needs to be assessed by evaluation against ground observations. The SKYNET (Sky radiometer network) network has been established for validating the JAXA GLI (Global

Imager) products (Takamura et al. 2009), as well as those from the NASA AERONET (Aerosol Robotic Network) (Holben et al. 1998). The main instrument of the network for both products is, a radiometer which can measure sky brightness at several wavelengths relevant for obtaining information on the radiative characteristics of aerosols. Since directional sky radiances are strongly dependent on particulate matter suspended in the atmosphere (Nakajima et al. 1983), aerosol parameters have been derived under clear sky conditions and provided to the community and researchers (http://atmos3.cr.chiba-u.jp/skynet/data.html).

Spectral irradiance is useful for many fields not only of the atmospheric environment but also engineering targets. A Multi-Filter Rotating Shadow-band Radiometer (MFRSR) is one of the typical instruments utilized. It is frequently used to get simultaneous measurements of spectral direct and diffuse radiation (Harrison et al. 1994) as described in Augustine et al. (2000). Another spectral radiometer MS-700 with a diffraction grating has been used to estimate aerosol parameters (Khatri et al. 2012). In all these instruments the shadow-band system plays a basic role to separate two components of irradiance, direct normal irradiance and diffuse horizontal irradiance, derived from the global irradiance measurements. This separation of observed irradiances can allow to estimate simultaneously optical characteristics of aerosols and clouds as well as characteristics of precipitable water (Alexandrov et al. 2009) and/or ozone amount in the atmosphere.

Observations from radiometers can be affected by errors such as calibration accuracy, temperature dependence and other sources under various observational conditions even if there is no human error in operation. When using the shadow-band system, another source of error is the analysis procedure. The issue addressed in this analysis is how to compensate correctly for the scattered radiation shadowed by a band. The accuracy of the aerosol/cloud products retrieved from these kinds of instrument data will be sensitive to such correction schemes.

This paper discusses errors originating from the shadow-band measurement system when only the nominal geometrical correction method is used. In this simulation analysis typical aerosol models are used for qualitative and quantitative estimation of irradiance. The effects of the estimation error of the optical depth as well as the direct and diffuse solar irradiance are also discussed.

2. Instrument and analysis procedure

At several sites of the SKYNET observation network, we have installed spectral radiometers (MS-700 manufactured by EKO Instruments Co., Ltd.) with a shadow-band system (MB-22), shown in Fig. 1. MS-700 measures global solar radiation spectrally using an inline CCD (Charge-Coupled Device) sensor with a grating connected to a diffuser and a glass fiber tube for the solar input. MB-22 can be used to separate direct normal irradiance (spDNI) from the global horizontal irradiance (spGHI) and estimate diffuse horizontal irradiance (spDHI). The rotating axis of the band is set in parallel with the north-south direction. It is inclined with 15 deg from the horizontal level (diffuser level) to the south side for northern latitudes to avoid the effect of the radiation reflected from the driving unit itself. The view angle of the shadow-band from the diffuser is 8.6 deg in width. The detailed specifications are given in Tables 1a and 1b, respectively. The basic concept is similar to the MFRSR (Harrison et al. 1994). These are unique and powerful tools for simultaneous observation of spGHI and spDNI with a single sensor unit, and are relatively low cost and easy to operate.

However, when estimating the spDNI derived from the observed spGHI, the biggest issue is the accuracy of the spDNI caused by uncertain estimate of the scattered light around the sun of the shadow-region. This depends on the aerosol size distribution and its optical depth, and consequently it is not easy to compensate for the effect of collecting more reliable spDNIs. Also, the error of the estimate of the spDNI is affected by instrumental conditions such as the rotating system, and the band width. We analyze the errors in the estimation of irradiances, spDNI and spDHI, due to the aerosol type and density using a MS-700 shadow-band system.

In normal operation, the band can move in four steps for radiation compensation. First, it stays at a level lower than the horizontal surface of the diffuser/sensor to get the spGHI (I_{obs1}). Then, it moves to the second position that is, at 10 deg behind from the center of the sun (I_{obs2}). After obtaining these data, it moves again to receive only the diffuse radiation (I_{obs3}) without the direct solar radiation. At this moment, the center of the band is partly normal to the solar direction. Finally, the shadow-band is set at 10 deg ahead of the sun (I_{obs4}). By using this sequence, a set of four data can be obtained for one scan. The second and fourth data are used to partially compensate for the excess diffuse radiation blocked by the band during the third (direct blocked) measurement.

The observed data, $I_{obs1} \sim I_{obs4}$, are described as follows,

$$I_{obs1} = \gamma_1 F_{dir} \mathrm{COS}(\theta_0) + \gamma_2 F_{dif}, \quad (1)$$

$$I_{obs2} = \gamma_1 F_{dir} \mathrm{COS}(\theta_0) + \gamma_2 (F_{dif} - \Delta F_2), \quad (2)$$

$$I_{obs3} = \gamma_2 (F_{dif} - \Delta F_3), \quad (3)$$

$$I_{obs4} = \gamma_1 F_{dir} \mathrm{COS}(\theta_0) + \gamma_2 \left(F_{dif} - \Delta F_4\right), \quad (4)$$

where variables and coefficients are defined as:

F_{dir} : Direct normal irradiance (spDNI),

F_{dif} : Diffuse horizontal irradiance (spDHI),

ΔF_i : Diffuse radiation shadowed by band at the position i=2 to 4 corresponding to $I_{obs2} \sim I_{obs4}$,

θ_0 : Solar zenith angle,

γ_1 : Correction coefficient for spDNI. It is due to the imperfect cosine response of the detection system, namely the cosine error, which depends only on the solar incident angle, not on the atmospheric particulate matters,

γ_2 : Correction coefficient for spDHI. It depends on particulate matters in the atmosphere and the cosine error.

In the above equations, we omit a suffix of wavelength dependency for simplicity. From these equations, spDNI and spDHI are:

$$\gamma_1 F_{dir} \mathrm{COS}(\theta_0) = I_{obs1} - I_{obs3} - \gamma_2 \Delta F_3 \ , \tag{5}$$

$$\gamma_2 F_{dif} = I_{obs3} + \gamma_2 \Delta F_3 \, . \tag{6}$$

In order to focus on the band effects, hereafter, correction coefficients, γ_1 and γ_2 are assumed to be 1.0. It should be noted that, practical diffuser/sensors have imperfect cosine law ($\gamma_1 \neq 1$) even if only a little. When the variable ΔF_3 can be estimated accurately under certain conditions, Eqs. (5) and (6) can provide correct spDNIs and spDHIs, as well as spGHI. In the usual measurements, however, this cannot be made clear. So, the unknown variable ΔF_3 is approximated by following equations,

$$\Delta F_3 \equiv C_{fwd} \ \frac{\Delta F_2 + \Delta F_4}{2}, \tag{7}$$

where,

$$\frac{\Delta F_2 + \Delta F_4}{2} \cong I_{obs1} - \frac{I_{obs2} + I_{obs4}}{2} \quad .$$

The correction coefficient C_{fwd} in Eq. (7) is a correction factor due to a stronger forward scattering ΔF_3 than ΔF_2 or ΔF_4. This depends on the directional pattern of the diffuse solar radiation. Therefore, the variation of C_{fwd} should be evaluated by changing the size distribution and the optical depth of aerosols. In practice, there are other reasons: one is, the difference of the solid view angles for each band position due to the band-driving geometry; the other is, the difference of the cosine effect. So, each diffuse irradiance, ΔF_i is inherently different. As expected, these effects increase with the decreasing solar altitude.

Using Eqs. (5), (6) and (7) we obtain:

$$F_{dir}\mathrm{COS}(\theta_0) = (1 - C_{fwd})I_{obs1} - I_{obs3} + C_{fwd}\left(\frac{I_{obs2} + I_{obs4}}{2}\right), \qquad (8)$$

$$F_{dif} = C_{fwd}I_{obs1} + I_{obs3} - C_{fwd}\left(\frac{I_{obs2} + I_{obs4}}{2}\right). \qquad (9)$$

In common data analysis practice, the correction coefficient, C_{fwd} is assumed to be 1 due to the lack of information on the correction. Consequently, the relative errors in spDNI and spDHI are:

$$Err_{spDNI} = \frac{F_{dir.est} - F_{dir}}{F_{dir}} = \frac{\frac{\left[-I_{obs3} + \left(\frac{I_{obs2} + I_{obs4}}{2}\right)\right]}{\cos(\theta_0)} - F_{dir}}{F_{dir}}, \quad (10)$$

$$Err_{spDHI} = \frac{F_{dif.est} - F_{dif}}{F_{dif}} = \frac{I_{obs1} + I_{obs3} - \left(\frac{I_{obs2} + I_{obs4}}{2}\right) - (F_{glb} - F_{dir}\cos(\theta_0))}{F_{glb} - F_{dir}\cos(\theta_0)}. \quad (11)$$

Based on the above, we estimate the band-shadowing effects and discuss errors on the spDNI and spDHI through simulation of this shadow-band system, using well-known aerosol types. At the same time, the error ($\Delta\tau$) in the optical depth can be estimated, as follows:

$$\Delta\tau = -\frac{1}{m}\ln\left(\frac{F_{dir.est}}{F_{dir}}\right). \quad (12)$$

The simulation is performed only at a wavelength of 500 nm because it is sufficient for obtaining trends of the estimation error of spDNI and spDHI due to the shadow-band system.

3. Simulations

Two step simulations are carried out. In the first step, the performance of the shadow-band system is examined precisely by using an isotropic sky brightness, and the reduction of the diffuse irradiance by band blockage is calculated for each of the three steps around the sun position. In the second step the total observation errors are estimated by introducing realistic atmospheric models with several aerosol types. The key is to obtain the accurate diffuse irradiance shadowed by each band position.

In order to achieve a realistic performance, instrumental and operative parameters for the MB-22 are those used in routine operations. In the simulation, it is assumed that the band movement can be perfectly followed by the accurate solar position without any mechanical error. The band rotates and stops regularly following the observation sequence, as described in section 2.

Irradiances incident to the diffuser/sensor are simulated under four aerosol conditions in the atmosphere as the most sensitive parameters. The basic atmospheric model selected is "Mid Latitude Summer" developed by McClatchey et al. (1972) with a surface pressure of 1013.25 hPa. Precipitable water content and ozone amount are somewhat different from the original ones, but these have no effect in this simulations and ozone has a weak absorption. Other minor gases are default in the atmospheric model. Four typical aerosol models are adopted. These are described in Shettle and Fenn(1979). These aerosol models have a function of modification of the size distribution by hygroscopic growth of aerosol particles (Hanel 1976). This function affects the Angstrom Exponent through changes of the aerosol size distribution, as well as the simulated irradiances. In order to estimate quantitatively the effects of the analysis method for the shadow-band technique, the aerosol optical depth (AOD) ranges from 0.001 to 2.0 at 500 nm (Table 2). Radiative transfer calculations are performed by the SBDART model, which is based on a scheme of a discrete ordinate method (Ricchiazzi et al. 1998). Radiance output of scattered solar radiation is for 1 deg resolution at zenith and azimuth direction for the sky dome. The integration over the region shadowed by each band is performed for every 0.1 deg step, by using the quadratic interpolation of the original 1-deg data base.

A band slant angle is defined by an angle formed by two planes, the band plane and the vertical plane including the north-south direction. It is a unique instrumental parameter, compared with the solar zenith and azimuth angle. The location and the date for the calculation are given in Table 2. These are not essential for the results. Sky patterns of brightness are calculated for every 15-minute step from 5:00 to 19:00.

4. Simulation results and discussion

4.1 Effects of shadow-band

First, we simulate accurately the movement of the shadow-band. Figure 2 shows examples for two times, 05:00 (Left) and 12:00 (Right) on Jun 22, 2016. These examples in the polar coordinate show that the azimuthal angle is measured clockwise, that is the north at the top, and 90 deg at the east, and the zenith angle is in the radial direction. Outer black circles in both panels mean the horizon with a zenith angle of 90 deg. Three closed lines colored blue, black and red, show band edges corresponding to band positions, 2, 3 and 4, respectively. Small red dots in the band position 3 demonstrate the solar position at respective times. Parts of each band are located below the horizon of the diffuser/sensor. Consequently, the effective field-of-view angles (FOV) for each band position are quite different when the sun is close to the horizon. From these figures, it is clear that the difference between ΔF_2 and ΔF_4 is geometrically increasing with the lower band/solar position. Figure 3a indicates the time series of the FOV of the sensor towards each band and their false irradiances corresponding to each band movement. In the figure, the input radiance is assumed to be isotropic. Therefore, geometrical errors can be estimated quantitatively for the system. The upper three curves (Right scale) show trends of each FOV for each band movement, and the lower ones (Left scale) are false irradiances in arbitrary unit. The patterns of FOV variation are relatively flat about the local noon as expected, and the irradiance patterns are changing with time, because the cosine effect to the received irradiance is clearly reflected. In both cases these patterns are symmetric about the local noon.

The correction error for the shadow region of the band position 3 is dependent on the value of C_{fwd} in Eq.7. Before estimating the impacts by using realistic aerosol types, Figure 3b shows the diurnal variation of ΔF_3 and ΔF_{mean} (equal to $\frac{\Delta F_2 + \Delta F_4}{2}$) for isotropic inputs. In the figure, the relative error (RE) between them, $\frac{\Delta F_{mean} - \Delta F_3}{\Delta F_3}$, is also plotted with time. Less than 2 % RE is shown around the relatively stable period with time, and then in the outer region it rapidly increases. Figure 3c plots show the variation of RE as functions of the solar zenith and band-slant angle. This fundamental error due to the cosine and geometric pattern (FOV difference) of each band position should be considered when processing observations. From the simulation with isotropic radiation input, a valid restriction condition in data analysis should be assumed to obtain reliable spDNI and spDHI. Accordingly we adopt the slant angle of the band (“Band slant angle” in Fig. 3c) as a common index for a valid evaluation.

The restriction for the fundamental error in the simulation is set to be 2 %. It means that the value of C_{fwd} corresponds to 1.02. Based on Figure 3c, it would translate to about 72 deg in band slant angle. The solar zenith angle is about 69 deg in this case and the corresponding relative airmass is about 2.8 as a limiting edge, as shown in Fig. 3c. We discuss, within these criteria, the error estimation, that ranges from 6:15 to 17:00 for the day (June 22).

When using this rotating shadow-band system, such fundamental errors are certain to happen. In addition, errors caused by actual observations and their analysis must be considered as well as the insufficient correction of forward scattering.

4.2 Simulation using typical aerosol types

In our simulations four typical aerosol types are introduced, as shown in Table 2. These have been modeled by Shettle and Fenn(1979), and already built in the SBDART code. These types do not necessarily cover all types of various aerosols in the real atmosphere, e.g., desert aerosol (Wandinger et al. 2016). However, they are sufficient for illustrating typical effects of different aerosols. Table 3 tabulates aerosol parameters such as single scattering albedo (SSA), asymmetry factor (ASY) at 500 nm and Angstrom Exponent (AE) as used in the simulation.

Two examples for different times, 08:00 and 11:45 are shown as sky brightness patterns in Figs.4a and 4b, respectively. These are shown only for the Oceanic aerosol type, for simplicity. The upper panels, (i) to (iv) in both figures indicate radiance patterns ($W/m^2/sr/um$) with different AODs, 0 (Rayleigh), 0.01, 0.1, and 1.0, and the lower ones, (v) to (viii) are for irradiance patterns ($W/m^2/um$) for unit solid angle. Solar positions are expressed as a small red dot in each panel. As a reference, band positions at the time are also displayed. It should be noted that the color code is different between the upper and lower panels.

It is clear that, the Rayleigh atmosphere has no strong forward scattering as expected, and it increases rapidly around the sun with increasing AOD. These patterns are different for different aerosol types not shown here, but basic trends are similar to each other. Irradiance patterns of the lower panels are more concentric compared with radiance patterns, because of the cosine effect. Such a concentric pattern is gradually distinctive with increasing solar altitude, as shown in Fig.4b. It is easily understandable that the difference in each shadow region must be dependent on the band slant angle and AOD.

Diffuse irradiances shadowed by each band are calculated as ΔF_2 to ΔF_4. An example is shown in Fig. 5a. It has Oceanic aerosol type with AOD of 0.2. The lower light blue line in Fig. 5a indicates the relative difference (right scale) in the correction method. This curve is stable for smaller zenith angles and rapidly changing with time near the sunrise and sunset. Figure 5b shows the change of C_{fwd} as functions of band slant angle and solar zenith angle for a period of the limited fundamental error of less than 2%. The maximum value of C_{fwd} reaches about 1.36 for AOD of 0.2. The three-dimensional pattern of the C_{fwd} variation is shown as a function of AOD and time for the Oceanic aerosol type in Fig. 6a. The diurnal variation is not the same for different AODs. The most remarkable feature in the pattern is the peak values for usual AOD ranges. It is due to the related variation between incident direct and diffuse solar radiation with AOD changes. When the AOD gradually increases, the diffuse radiation also increases till about 1 and then over this point it decreases because of the rapid decrease of the direct solar radiation. Figure 6b shows examples of this variation of shadowed irradiances as a function of AOD x SSA x Airmass. The correction coefficients C_{fwd} are also plotted by dash-dotted lines in the figure to understand the relation between them. The peak positions of C_{fwd} are shifted from the irradiance ones.

The saddle pattern in Fig.6a is almost the same as the other three types except for their magnitudes. Figure 6c depicts the variation of C_{fwd} for different aerosol types with a variation of AOD x SSA, where these patterns are almost same including each peak point except for the magnitude. These are the daily mean values with the standard deviation for the limited time domain. Aerosol impacts are clearly seen in the variation of C_{fwd} from these figures. The peak point of C_{fwd} for AOD (or AOD x SSA) is not the same as that for the diffuse radiation, but the trend is similar as the pattern of the shadowed diffuse radiation. As expected, the Oceanic type shows the largest value of C_{fwd} among the four aerosol types, because of its larger particles. Based on this, Figure 6d plots shows the relation between Angstrom Exponent (AE) and C_{fwd}, with AODs ranging from 0.01 to 1.0. The smaller AE can give a bigger error in general. But it should be noted that the maximum value of C_{fwd} for each aerosol type is not the biggest AOD in the figure, because of its AOD dependency as shown in Fig.6c.

Errors in spDNI and optical depth estimation (Err_{spDNI} in Eq. 10 and $\Delta\tau$ in Eq. 12) can be derived using the simulated data. Figure 7 is an example of a diurnal variation for the Oceanic aerosol with AOD of 0.2. Large cat ears can be seen in the Err_{spDNI} around the time of sun rise and set due to unbalanced FOV of each band. These are rejected automatically when analyzing data, based on the reasoning described before. Therefore, the Err_{spDNI} ranges from 1.2 % to 4.1 % within the effective domain of the band slant angle (or time) in this example. And the $\Delta\tau$ induced from the spDNI error is about -0.011 to -0.014 for AOD of 0.2. These errors might not be serious but are not negligible. The relatively small effects to spDNI and τ despite the large correction coefficient C_{fwd} is because part of the corrected irradiance in the diffuse radiation is much smaller than the spDNI value itself.

Figure 8a depicts the same error, Err_{spDNI} as a function of AOD x SSA for four aerosol types. The magnitude of Err_{spDNI} is different for each aerosol type as expected, even if each aerosol type has the same AOD. It can increase with AOD increasing. However, this can turn into a decreasing trend depending on the parameter of AOD x SSA x Airmass. Examples with AOD of 1.0 are shown in Fig.8b. It is clear that, the lines of Err_{spDNI} show peaks dependent on the AOD x SSA x Airmass. As a reference, the estimated spDNIs are plotted as well as the true spDNI, in the figure. These lines of spDNIs almost overlap because of their small differences. While the magnitude of spDNI is consistently decreasing as well as the absolute error of spDNI with the AOD increase, the relative error of spDNI Err_{spDNI} is increasing for small values of AOD x SSA x Airmass and then decreasing over a certain value depending on AOD. Therefore, the Err_{spDNI} changes with a similar pattern to C_{fwd} in Fig. 6c. A part of such variations is included in the rightmost points at AOD=1.5 of Fig.8a. Namely, the Err_{spDNI} varies from about 5% to 11% at AOD=1 of four aerosol types, and from about 2% to 5% at AOD=0.5. It is also plotted as a function of C_{fwd} as shown in Fig.8c. Seven AODs are used in the figure, the same as for Fig. 8a. The error bars for each line are also the same as before. The upper ends of each line in Fig.8c show values for AOD=1.5, and the lower left side is for AOD=0.01.

Based on these features, the estimation error ($\Delta\tau$) in optical depth can be retrieved simultaneously, as shown in Figs. 9a and 9b. The relative error $\Delta\tau/\tau$ is dependent on the magnitude of AOD as well as the aerosol type. These reflect the trend of Err_{spDNI}, as expected. As seen in Fig.9a, the relative errors $\Delta\tau/\tau$ of the daily average, range from about 3% to 4% or less for Tropospheric, Rural and Urban types, and less than 6% for Oceanic type at AOD of 1.0. Right ends of each line are for AOD of 1.5. Larger airmasses have larger errors than the averages. Figure 9b shows the relation between $\Delta\tau/\tau$ and C_{fwd}. In the figure, the lowest (negatively biggest) ends of each line are for AOD=1.5 and the uppermost points are for AOD=0.01. This corresponds to Fig. 8c. It is clear that, depending on their aerosol type, the AOD change strongly affects the estimation error. This suggests that the $\Delta\tau/\tau$ is also dependent on the Angstrom Exponent. Figure 10 shows their relation. The dependency on AE is plotted with 6 AOD parameters, 0.01 to 1.0, for each aerosol type. The smaller AE can give a larger error, as a rough standard. For example, the optical depth estimation under the rural or urban atmosphere with usual AOD might be expected to show about 3 to 4 % relative error at most. Oceanic aerosol type is a little far from other three types because of rich coarse mode particles by hygroscopic growth. Based on this figure, radiation measurements in the atmosphere containing rich particles of coarse mode like oceanic or desert dust particles, should be carefully analyzed. The information of AE is a good indicator for the rough error estimation, which can be deduced by spectral observation.

SSA is one of the most important parameters on the aerosol impact in climate research. Diffuse radiation measurements can provide the possibility to determine the SSA (Khatri et al., 2012). Consequently, the spDHI can be estimated by using Eq. 9. In this case, the relative error Err_{spDHI} is obtained by using Eq. 11. Figures 11a and 11b show the Err_{spDHI} estimate as functions of

AOD x SSA and C_{fwd}, respectively. The maximum error points (lowest of each line in the figure) for each aerosol type are visible. For example, the Oceanic aerosol type shows a Err_{spDHI} of about 4 % for the worst case. In general, these points are mainly dependent on the aerosol size distribution through a correction coefficient C_{fwd}. Figure 11b shows the relation between Err_{spDHI} and C_{fwd}. It shows a unique feature, of the linear relation between them. Based on this, a rough estimate of the relative error could be performed. The Err_{spDHI} can be estimated by the AE as shown in Fig. 12, for AOD parameter ranging from 0.01 to 1.0. The error is strongly dependent on AOD as well as on the AE index. While the smaller AOD can give a smaller relative error in spDHI, the largest error shows AOD = 0.5 (light blue line in Fig.12), as also seen in Fig. 11a. This is due to the dependence of the relation between AOD and the corresponding diffuse radiation.

The errors discussed above are summarized in Table 4 for two typical AODs of 0.5 and 1.0. Each value in the table is a daily mean with the standard deviation for the effective time domain. These AODs are considered to be under normal atmospheric condition. Such errors might occur when using a common correction technique, $C_{fwd} = 1$. Therefore, if an appropriate value of C_{fwd} is introduced in the actual analysis, these errors might shrink. These results can help to improve the analysis method for obtaining more accurate aerosol parameters.

5. Conclusions

A spectral radiometer with a shadow-band system is a unique and powerful tool for various fields, such as air quality, atmospheric and biological environment as well as solar radiation. The objective of a rotating shadow-band is to separate spectral direct (spDNI) and diffuse (spDHI) irradiances from directly observed global spectral irradiances (spGHI). When performing the separation, a suitable correction scheme is required for the diffuse irradiance shadowed by the band. The accuracy of the estimated irradiances is dependent on this correction scheme. Based on the most popular correction technique for this system, errors in spDNI and spDHI estimation are discussed in detail using realistic instrumental parameters with four typical aerosol types.

The key issue is the accuracy of the correction of diffuse irradiances shadowed by the band. Even if the instrumental system has no error such as cosine characteristics of the sensor/diffuser and calibration including observation errors, the usual correction method can give errors because of the under-estimate of the forward scattering and asymmetric positions of the shadow-band for correction. First, fundamental errors based on the correction method itself are estimated by using uniform isotropic radiance as input. When the slant angle of the shadow-band is less than 72 deg with realistic parameters of the system, the relative error in the diffuse irradiance of shadow-region between the true value and its approximation is within 2%. This error is inevitable when using this system. It can be caused by the difference of the shadow-band positions for correction, which equals the difference of the cosine effect of the diffuser/sensor. Over the 72 deg, the error rapidly increases, so that the estimated spDNI and spDHI might not be usable. It should be noted that the value of the limited angle of the shadow-band is dependent on the parameters used in the shadow-band system.

The relative errors in the estimated spDNI and spDHI, using realistic atmospheres with four typical aerosol types, Rural, Urban, Ocean and Troposphere, as compiled by Shettle and Fenn (1979), and considered within the basic error of 2 %. The aerosol optical depth (AOD) at 500 nm in the simulation yields eleven cases from 0.001 to 2.0, which can cover usual atmospheric conditions. As seen from the simulation, the correction coefficient C_{fwd} for the forward scattering region of the shadow-band is strongly dependent on AOD (or

AOD x SSA). It increases and then reaches a peak and after that it decreases when the AOD (or AOD x SSA) is increasing. These phenomena originate from the relation between spDNI and spDHI with the AOD change. The coefficient C_{fwd} for the Oceanic aerosol type shows larger values than the other aerosol types because it is enriched with coarse particles. This trend is confirmed by the correlation with the Angstrom Exponent.

The relative error in the spDNI estimation shows a variation from 2% to 5% at AOD=0.5 and from 5% to 11% at AOD=1 of the four aerosol types. Based on these results, the relative error in the optical depth estimation varies within, 2% to 5% at AOD=0.5 for four aerosol types, almost the same as the spDNI estimation. On the other hand, the spDHI estimation has a unique error of about 4 % maximum for the AOD range of 0.1 to 1.0 for the Oceanic aerosol type. The AOD increase over the range is at the origin of the decrease in the spDHI error, and the error variation against C_{fwd} shows roughly a linear relationship with the weak aerosol type dependency.

These features can help to improve the accuracy of the spDNI and spDHI estimation.

Acknowledgements

This study is partly supported by a Grant-in-Aid for Scientific Research (C) 17K05650 from Japan Society for the Promotion of Science (JSPS), Japan Aerospace Exploration Agency (PI no. ER2GCF211, contract no. 19RT000370) , and “Virtual Laboratory for Diagnosing the Earth’s Climate System” program of MEXT, Japan.

The authors are grateful to Prof. R. Pinker of the University of Maryland for helpful discussions and comments of the manuscript. We would like to thank Prof. H. Irie of the Center for Environmental Remote Sensing, Chiba University for maintaining the SKYNET observation and data management, and Dr. Dim Jules Rostand for his careful reading and comments of the manuscript.

References

Alexandrov, M. D., B. Schmid, D. D. Turner, B. Cairns, V. Oinas, A. A. Lacis, S. I. Gutman, E. R. Westwater, A. Smirnov, and J. Eilers ,2009: Columnar water vapor retrievals from multifilter rotating shadowband radiometer data, *J. Geophys. Res.*, **114**, D02306, doi:10.1029/2008JD010543.

Augustine, J.A., J.J. Deluisi, and C.N. Long, 2000: SURFRAD – A national surface radiation budget network for atmospheric research, *Bull. Am. Meteor. Soc.*, **81**, 2341 – 2357.

Bi, J., J. Shi, Y. Xie, Y. Liu, T. Takamura, P. Khatri, 2014: Dust Aerosol Characteristics and Shortwave Radiative Impact at a Gobi Desert of Northwest China during the Spring of 2012, *J. Meteor. Soc. Japan*, **92A**, 33-56. DOI:10.2151/jmsj.2014-A03

Hanel, G., 1976: The Properties of Atmospheric Aerosol Particles as Functions of the Relative Humidity at Thermodynamic Equilibrium with the Surrounding Moist Air, *Advances in Geophysics* (Eds.: H.E. Landsberg and J. Van Mieghem), **19**, 73-188.

Harrison, L., J. Michalsky, and J. Berndt, 1994: Automated multifilter rotating shadow-band radiometer: An instrument for optical depth and radiation measurements. *Appl. Opt.*, **33**, 5118–5125.

Holben, B.N.,T.F.Eck, I.Slutsker, D.Tanré, J.P.Buis, A.Setzer, E.Vermote, J.A.Reagan, Y.J.Kaufman, T.Nakajima, F.Lavenu, I.Jankowiak, A.Smirnov, 1998: AERONET—A Federated Instrument Network and Data Archive for Aerosol Characterization, *Remote Sensing of Environment*, **66(1)**, 1-16, doi.org/10.1016/S0034-4257(98)00031-5.

IPCC, 2014: *Climate Change 2014*: Synthesis Report. Contribution of Working Groups I, II and III to the Fifth Assessment Report of the Intergovernmental Panel on Climate Change. Core Writing Team, R. K. Pachauri, and L. A. Meyer (eds.), IPCC, Geneva, Switzerland, 151 pp.

Khatri, P., T. Takamura, A. Yamazaki, and Y. Kondo, 2012: Retrieval of Key Aerosol Optical Parameters from Spectral Direct and Diffuse Irradiances Observed by a Radiometer with Nonideal Cosine Response Characteristic. *J. Atmos. Ocean. Tech.*, **29**, 683 – 696. DOI: 10.1175/JTECH-D-11-00111.1.

Koepke, P., J. Gasteiger, and M. Hess, 2015: Technical Note: Optical properties of desert aerosol with non-spherical mineral particles: data incorporated to

OPAC, *Atmos. Chem. Phys.*, **15**, 5947–5956, doi:10.5194/acp-15-5947-2015.

Kim, D-H., B-J. Sohn, T. Nakajima and T. Takamura, 2005: Aerosol radiative forcing over east Asia determined from ground-based solar radiation measurements, *J. Geophys. Res.*, **110**, D10S22, doi:10.1029/2004JD004678,2005.

McClatchey, R. A., R. W. Fenn, J. E. A. Selby, F. E. Volz, and J. S. Garing, 1972: Optical properties of the atmosphere. 3rd ed. *AFCRL Environ. Res. Papers* **No. 411**.

Nakajima, T., M. Tanaka, and T. Yamauchi, 1983: Retrieval of the optical properties of aerosols from aureole and extinction data, *Appl. Opt.*, **22(19)**, 2951-2959.

Nakajima, T., S.-C. Yoon, V. Ramanathan, G.-Y. Shi, T. Takemura, A. Higurashi, T. Takamura, K. Aoki, B.-J. Sohn, S.-W. Kim, H. Tsuruta, N. Sugimoto, A. Shimizu, H. Tanimoto, Y. Sawa, N.-H. Lin, C.-T. Lee, D. Goto, and N. Schutgens, 2007: Overview of the Atmospheric Brown Cloud East Asian Regional Experiment 2005 and a study of the aerosol direct radiative forcing in east Asia, *J. Geophys. Res.*, **112**, D24S91, doi:10.1029/2007JD009009.

Ricchiazzi, P., S. Yang, C. Gautier, and D. Sowle, 1998: SBDART: A Research and Teaching Software Tool for Plane-Parallel Radiative Transfer in the Earth's Atmosphere. *Bull. Am. Meteor. Soc.*,**79**, 2101-2114.

Shettle E. P., and R. W. Fenn, 1979: Models for the Aerosols of the Lower Atmosphere and the Effects of Humidity Variations of Their Optical Properties, AFGL-TR-79-0214, Air Force Geophysics Lab., Hanscom, MA.

Stephens, G. D. Winker, J. Pelon, C. Trepte, D. Vane, C. Yuhas, T. L'Ecuyer, M. Lebsock, 2018: CloudSat and CALIPSO within the A-Train: Ten Years of Actively Observing the Earth System, *Bull. Amer. Meteor. Soc.*, **99 (3)**, 569–581. https://doi.org/10.1175/BAMS-D-16-0324.1

Takamura, T., H. Takenaka, Y. Cui, T. Y. Nakajima, A. Higurashi, S. Fukuda, N. Kikuchi, T. Nakajima, I. Sato, and R. T. Pinker, 2009:Aerosol and cloud validation system based on SKYNET observations: Estimation of shortwave radiation budget using ADEOS-II/GLI data, *J. Remote Sens. Japan*, **29**, 40-53.

Wandinger, U., H. Baars, R. Engelmann, A. Hünerbein, S. Horn, T. Kanitz, D. Donovan, G.-J. van Zadelhoff, D. Daou, J. Fischer, J. von Bismarck, F. Filipitsch, N. Docter, M. Eisinger, D. Lajas, T. Wehr, 2016: HETEAC: THE

AEROSOL CLASSIFICATION MODEL FOR EARTHCARE. EPJ Web of Conferences 119, 01004, ILRC27. DOI: 10.1051/epjconf/201611901004

List of Figures

Fig. 1 Observation system for spectral irradiance with shadow-band. The detailed specifications of MS-700 and MB-22 are tabulated in Tables 1a and 1b. The driving unit is installed with an inclined angle (rotating axis) of 15° to avoid the effect of light reflected by itself.

Fig. 2 Examples of shadow-band movement. The bands are projected on the polar coordinate. Blue, black and red curves show edge patterns of band positions 2, 3 and 4 respectively and, for different times: 05:00 and 12:00 JST of June 22, 2016. Small red dots in both circles mean the solar position. The outer circle shows the horizon (zenith angle is 90 deg.) of the sky. The band positions outside the circles are below the horizon.

Fig.3a Time series for each band, of the field-of-view angle (*FOV*), represented by the upper three solid curves and, the virtual radiation (ΔF) incident into a region shadowed by the band, represented by the lower three curves. The incident radiation is assumed to be unity, so these curves mean variations combined with the cosine characteristic and field view angle.

Fig.3b Time series of virtual radiation and the difference between the expected irradiance ΔF_3 (for isotropic radiation) and the mean irradiance approximated by both side ones (ΔF_2 and ΔF_4).

Fig. 3c Relative difference between the expected irradiance and the mean irradiance approximated by ΔF_2 and ΔF_4, as functions of the solar zenith and band slant angles. For less than 72 deg band slant angle, the fundamental error due to the cosine characteristic including the band geometry is about less than 2%. The relative airmass corresponding to the solar zenith angle is plotted as a reference.

Fig. 4a Examples of simulated sky brightness without direct solar radiation. Each brightness pattern corresponds to different AODs: 0 (Rayleigh atmosphere), 0.01, 0.1, and 1.0 respectively from left to right in two panels' series (upper and lower). The upper panels' series show the radiance pattern (W/m^2/sr/um) and the lower panels' series are the irradiance pattern

(W/m^2/um) for a unit solid angle. The solar position is θ_0 = 49.0, $\emptyset_0$ = 88.5 at 08:00 JST, which is plotted as a small red dot in each panel. It should be noted that, the color codes of the radiance and irradiance patterns are different. As a reference, band positions are shown in each pattern.

Fig. 4b Examples of simulated sky brightness. Same as Fig. 4a except for the time of 11:45 (θ_0 = 12.2, $\emptyset_0$ = 183.7).

Fig. 5a Simulated diffuse irradiance shaded by each band position, 2 to 4. The atmosphere is the oceanic aerosol type with AOD of 0.2. ΔF_3 corresponds to the position of shading the direct solar radiation. ΔF_2 and ΔF_4 show shaded irradiances for band position 2 (-10 deg) and position 4 (+10 deg) . ΔF_{mean} is the arithmetic mean of ΔF_2 and ΔF_4, and The Relative Difference is defined by (ΔF_{mean} - ΔF_3)/ ΔF_3.

Fig. 5b Correction coefficient C_{fwd} defined by ΔF_3/ ΔF_{mean} as a function of the solar zenith and band slant angles. Curves are plotted with a fundamental error of less than 2%.

Fig. 6a Variation of the correction coefficient C_{fwd} as a function of AOD and time. This 3-D pattern is for the Oceanic aerosol type. Other types show similar patterns except for their magnitudes.

Fig. 6b Examples of diffuse irradiance shadowed by a band and the corresponding C_{fwd}, as a function of AOD x SSA x Airmass. Solid and broken lines colored in blue (11:45) and orange (6:30) are true and approximated values, respectively. The ratios, C_{fwd} on the right scale are shown by dash-dotted lines.

Fig. 6c Variation of mean correction coefficient C_{fwd} as a function of AOD x SSA. Each value is averaged for the same AOD during a certain period, with a fundamental error of less than 2%. Each error bar is the standard deviation of the daily mean.

Fig. 6d Relation between C_{fwd} and Angstrom Exponent for four aerosol types. Error bars in each line are the same as in Fig. 6c.

Fig. 7 An example of diurnal variation of relative error (Err_{spDNI}) in spDNI and optical depth error ($\Delta\tau$), defined by Eqs. 10 and 12. These are plotted for the Oceanic aerosol type with AOD of 0.2.

Fig. 8a Estimation error in spDNI as a function of AOD x SSA for four aerosol types. Seven AODs are used for each aerosol type, such as 0.01, 0.05, 0.1, 0.2, 0.5, 1.0 and 1.5. The error bars are due to the daily variation for the effective time domain.

Fig. 8b Examples of spDNI and Err_{spDNI} as a function of AOD x SSA x Airmass for four aerosol types with AOD of 1.0. The estimated spDNIs (spDNI_est) for each aerosol type overlap on the same lines due to small differences. The patterns of Err_{spDNI} show peaks depending on the aerosol type.

Fig. 8c Relative error in spDNI as a function of C_{fwd}. Seven AODs are used as the same in Fig.8a for each aerosol type. The upper ends of each line are for AOD=1.5. The error bars are the same as in Fig.8a.

Fig. 9a Relative error in optical depth as a function of AOD x SSA. The four lines with error bars indicate different aerosol types for seven AODs, 0.01, 0.05, 0.1, 0.2, 0.5, 1.0 and 1.5. The rightmost ends of each line are for AOD=1.5.

Fig. 9b Estimation error in optical depth as a function of C_{fwd}. The four lines with error bars indicate different aerosol types for seven AODs, 0.01, 0.05, 0.1, 0.2, 0.5, 1.0 and 1.5. The lowest ends of each line are for AOD=1.5, and the smallest (upper) points are for AOD=0.01.

Fig. 10 Relation between $\Delta\tau/\tau$ and Angstrom Exponent.

Fig. 11a Relative error in spDHI estimation as a function of AOD x SSA. Each aerosol type shows the minimum points during a range of 0.1 to 1.0 AOD x SSA.

Fig. 11b Same as Fig. 11a except for as a function of C_{fwd}. The minimum point of the error for the Oceanic aerosol type corresponds to the maximum C_{fwd}.

Fig. 12 Relative error in spDHI estimation as a function of the Angstrom Exponent (AE) with different AODs, ranging from 0.01 to 1.0. Four aerosol types are shown corresponding to their AEs.

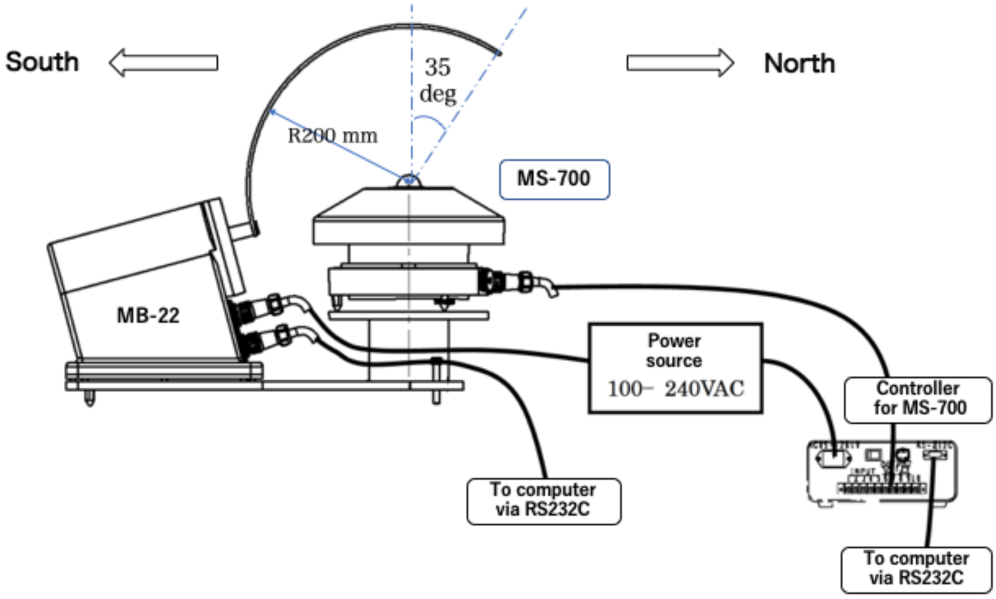

Fig. 1 Observation system for spectral irradiance with shadow-band. The detailed specifications of MS-700 and MB-22 are tabulated in Tables 1a and 1b. The driving unit is installed with an inclined angle (rotating axis) of 15° to avoid the effect of light reflected by itself.

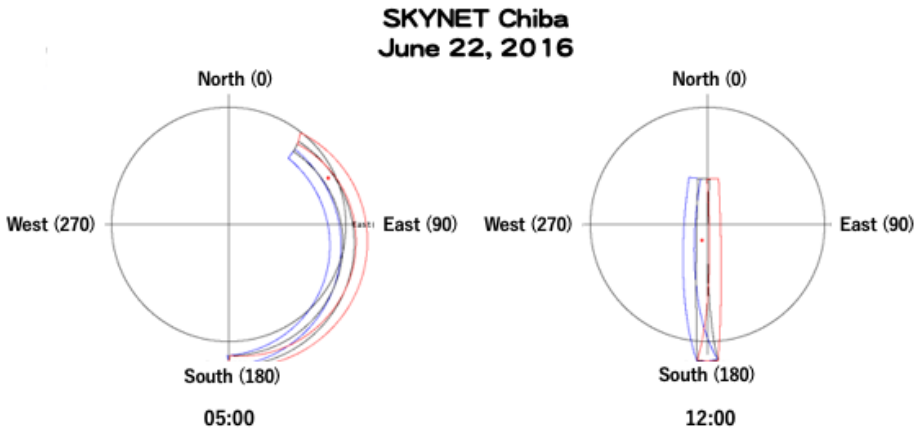

Fig. 2 Examples of shadow-band movement. The bands are projected on the polar coordinate. Blue, black and red curves show edge patterns of band positions 2, 3 and 4 respectively and, for different times: 05:00 and 12:00 JST of June 22, 2016. Small red dots in both circles mean the solar position. The outer circle shows the horizon (zenith angle is 90 deg.) of the sky. The band positions outside the circles are below the horizon.

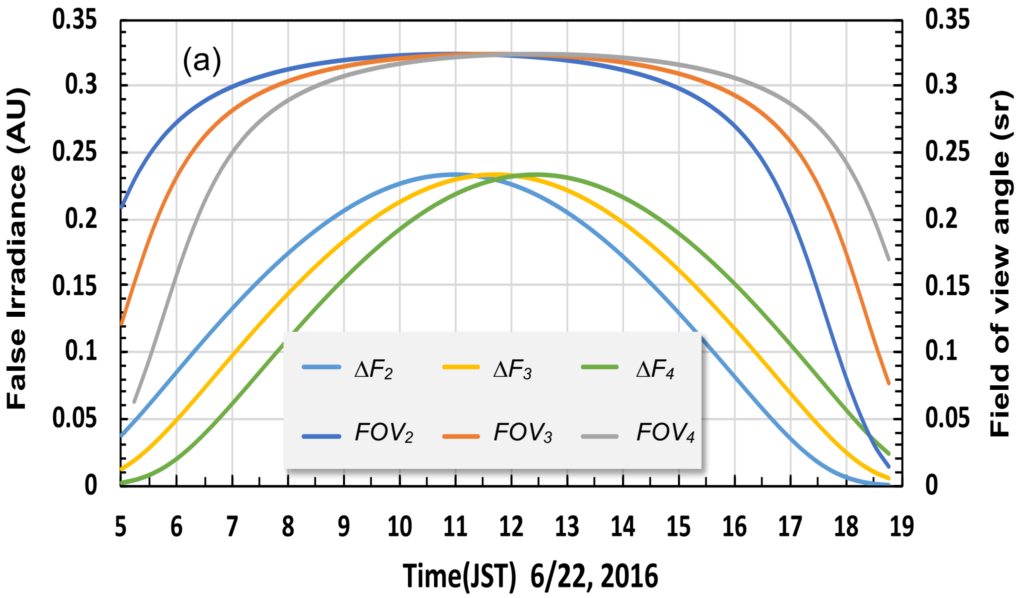

Fig.3a Time series for each band, of the field-of-view angle (*FOV*), represented by the upper three solid curves and, the virtual radiation (ΔF) incident into a region shadowed by the band, represented by the lower three curves. The incident radiation is assumed to be unity, so these curves mean variations combined with the cosine characteristic and field view angle.

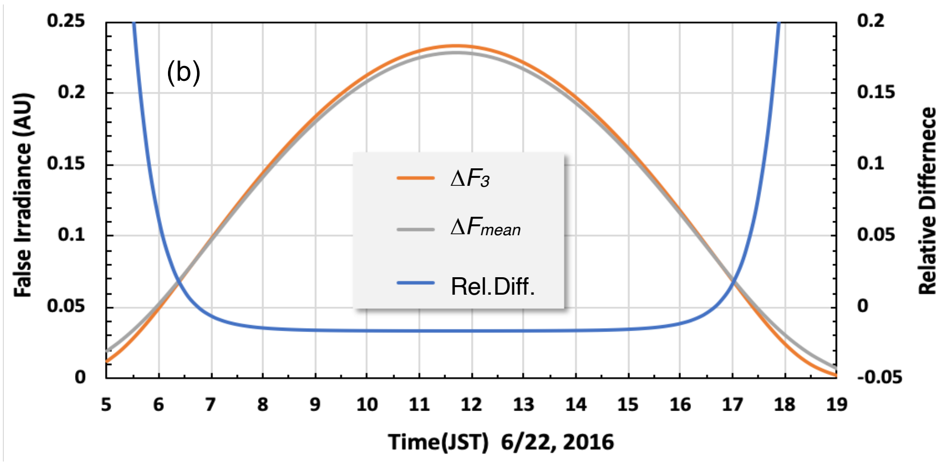

Fig.3b Time series of virtual radiation and the difference between the expected irradiance ΔF_3 (for isotropic radiation) and the mean irradiance approximated by both side ones (ΔF_2 and ΔF_4).

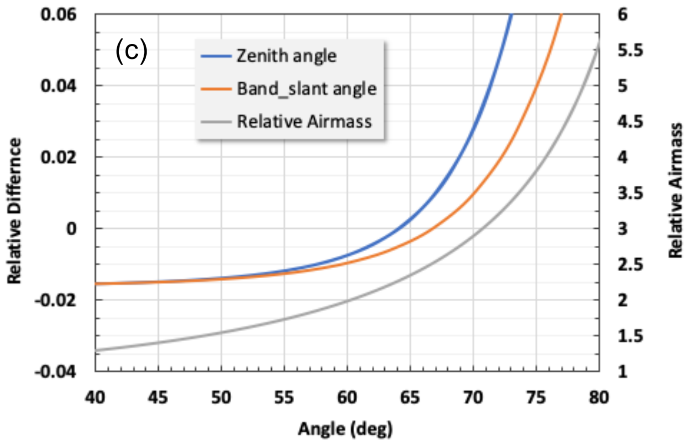

Fig. 3c Relative difference between the expected irradiance and the mean irradiance approximated by ΔF_2 and ΔF_4, as functions of the solar zenith and band slant angles. For less than 72 deg band slant angle, the fundamental error due to the cosine characteristic including the band geometry is about less than 2%. The relative airmass corresponding to the solar zenith angle is plotted as a reference.

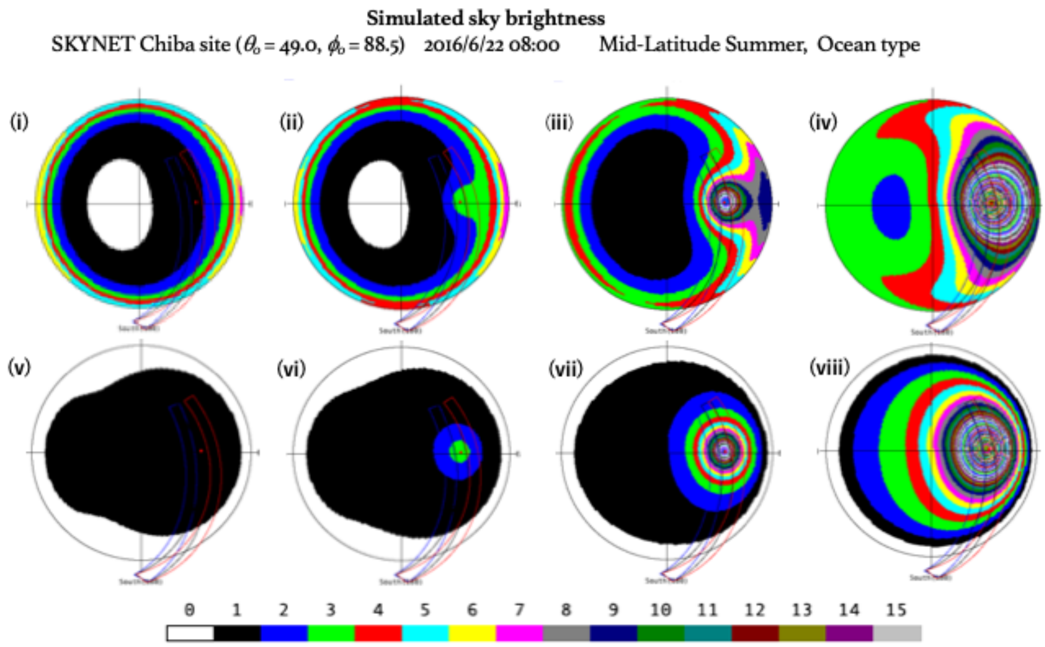

Fig. 4a Examples of simulated sky brightness without direct solar radiation. Each brightness pattern corresponds to different AODs: 0 (Rayleigh atmosphere), 0.01, 0.1, and 1.0 respectively from left to right in two panels' series (upper and lower). The upper panels' series show the radiance pattern (W/m^2/sr/um) and the lower panels' series are the irradiance pattern (W/m^2/um) for a unit solid angle. The solar position is θ_0 = 49.0, $\emptyset_0$ = 88.5 at 08:00 JST, which is plotted as a small red dot in each panel. It should be noted that, the color codes of the radiance and irradiance patterns are different. As a reference, band positions are shown in each pattern.

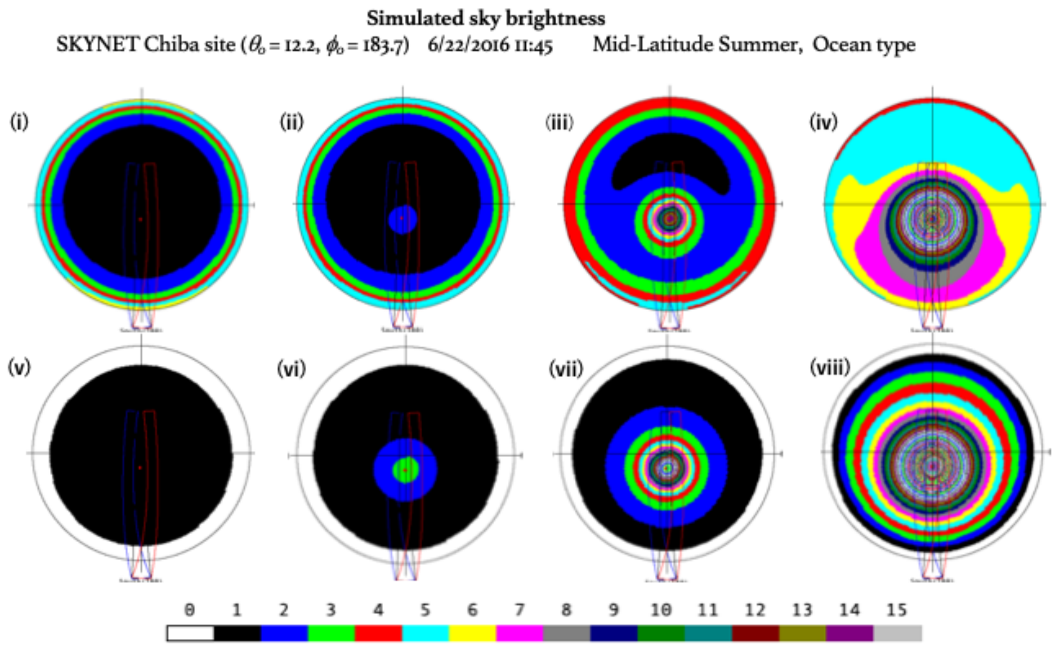

Fig. 4b Examples of simulated sky brightness. Same as Fig. 4a except for the time of 11:45 (θ_0 = 12.2, $\emptyset_0$ = 183.7).

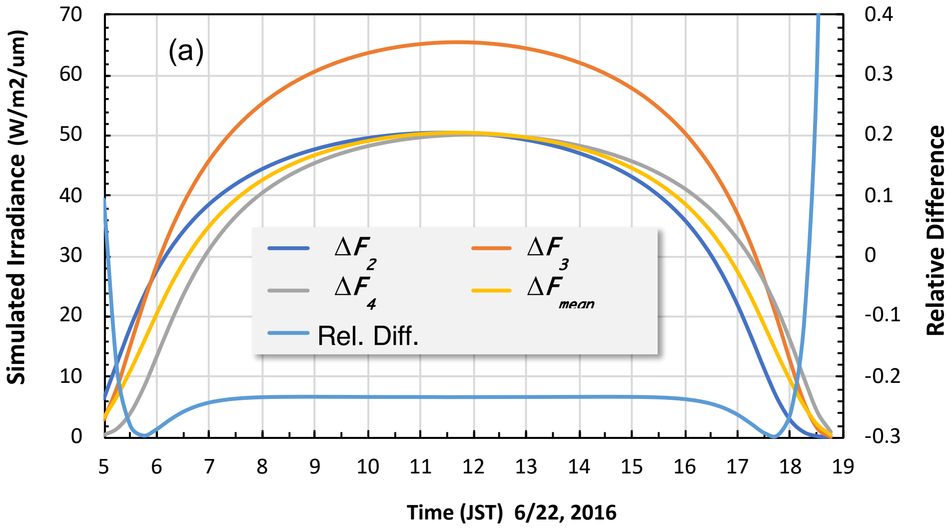

Fig. 5a Simulated diffuse irradiance shaded by each band position, 2 to 4. The atmosphere is the oceanic aerosol type with AOD of 0.2. ΔF_3 corresponds to the position of shading the direct solar radiation. ΔF_2 and ΔF_4 show shaded irradiances for band position 2 (-10 deg) and position 4 (+10 deg) . ΔF_{mean} is the arithmetic mean of ΔF_2 and ΔF_4, and The Relative Difference is defined by (ΔF_{mean} - ΔF_3)/ ΔF_3.

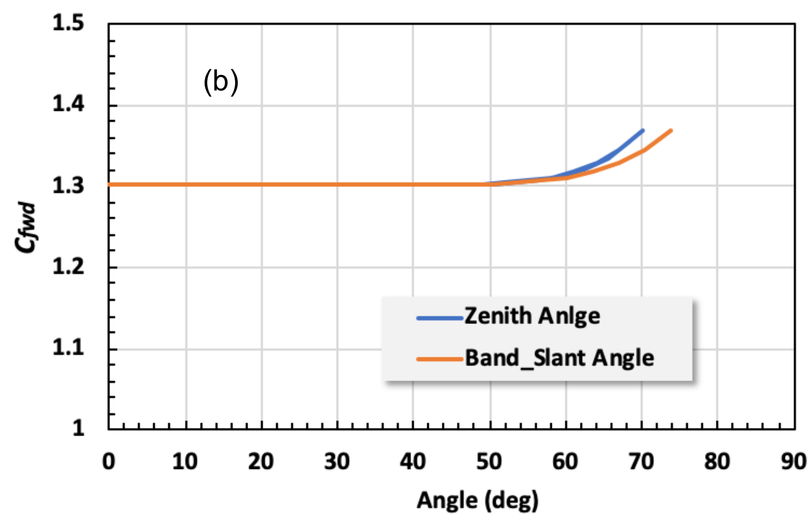

Fig. 5b Correction coefficient C_{fwd} defined by $\Delta F_3 / \Delta F_{mean}$ as a function of the solar zenith and band slant angles. Curves are plotted with a fundamental error of less than 2%.

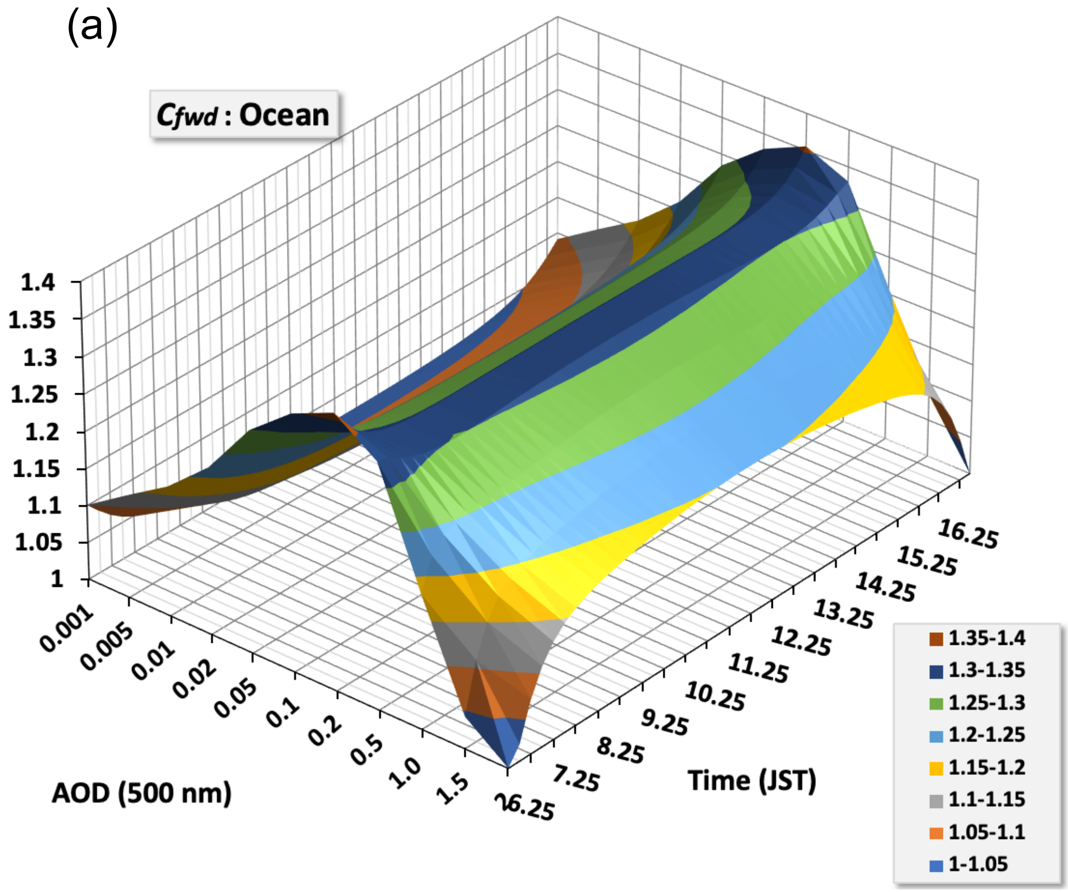

Fig. 6a Variation of the correction coefficient C_{fwd} as a function of AOD and time. This 3-D pattern is for the Oceanic aerosol type. Other types show similar patterns except for their magnitudes.

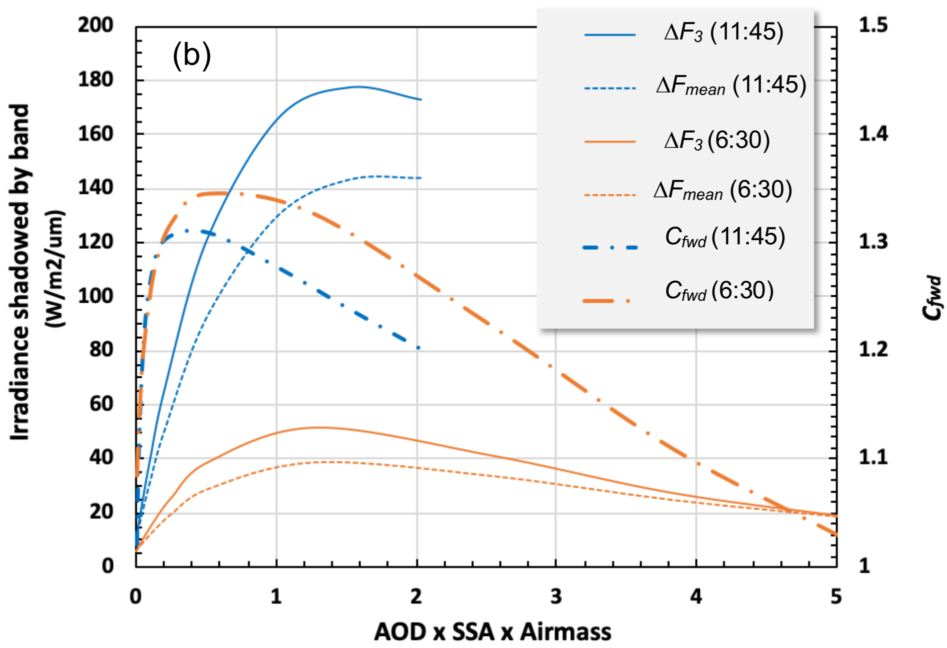

Fig. 6b Examples of diffuse irradiance shadowed by a band and the corresponding C_{fwd}, as a function of AOD x SSA x Airmass. Solid and broken lines colored in blue (11:45) and orange (6:30) are true and approximated values, respectively. The ratios, C_{fwd} on the right scale are shown by dash-dotted lines.

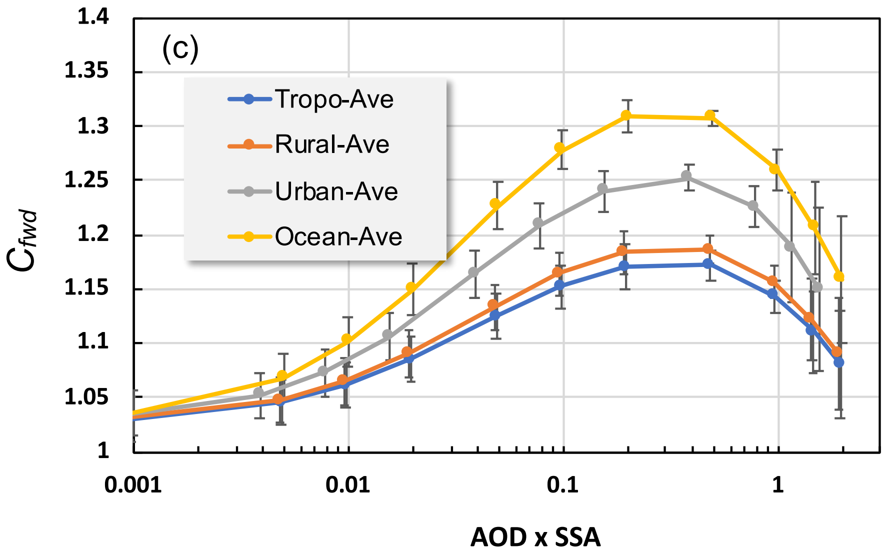

Fig. 6c Variation of mean correction coefficient C_{fwd} as a function of AOD x SSA. Each value is averaged for the same AOD during a certain period, with a fundamental error of less than 2%. Each error bar is the standard deviation of the daily mean.

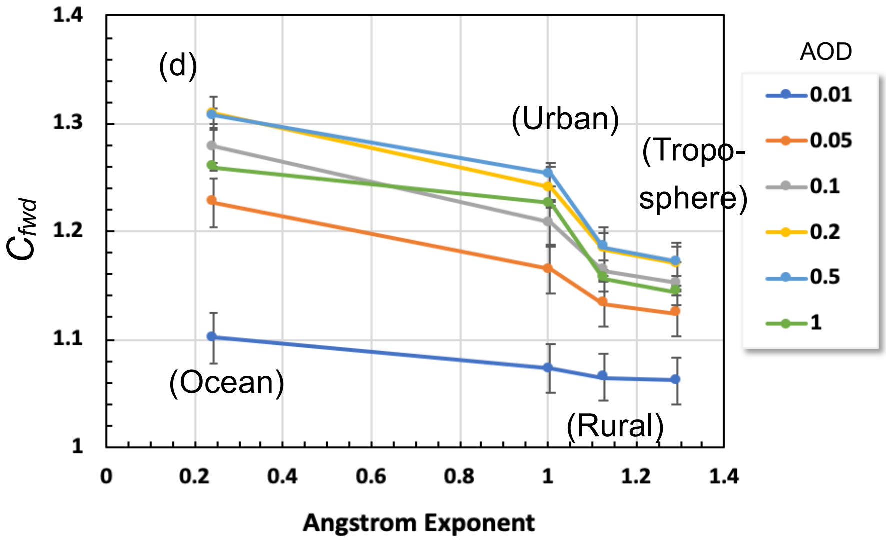

Fig. 6d Relation between C_{fwd} and Angstrom Exponent for four aerosol types.

Error bars in each line are the same as in Fig. 6c.

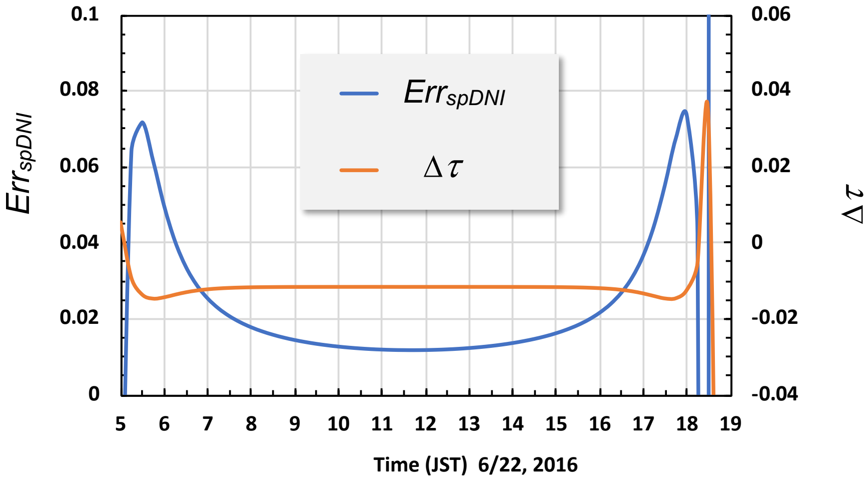

Fig. 7 An example of diurnal variation of relative error (Err_{spDNI}) in spDNI and optical depth error ($\Delta\tau$), defined by Eqs. 10 and 12. These are plotted for the Oceanic aerosol type with AOD of 0.2.

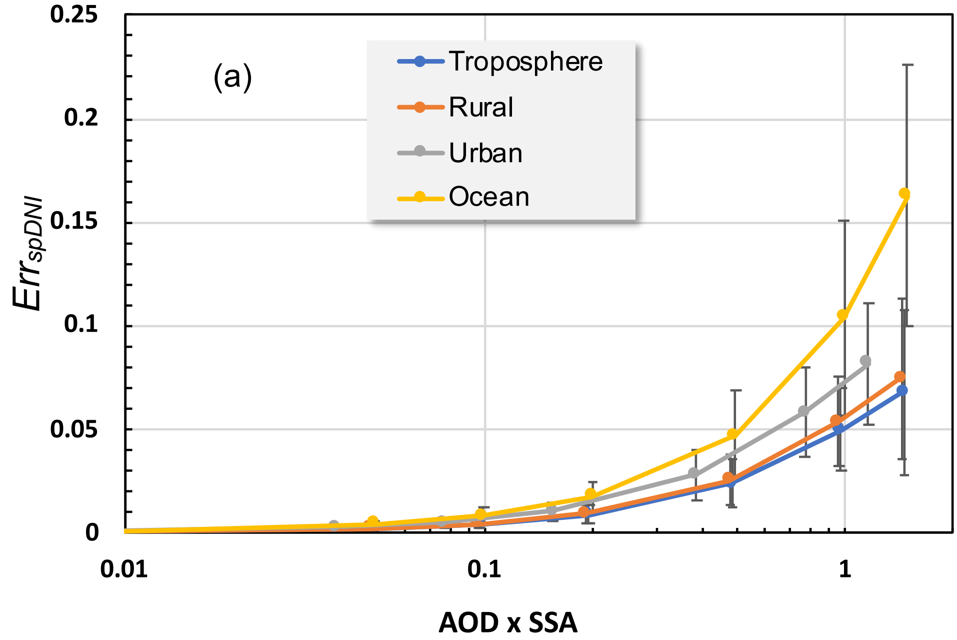

Fig. 8a Estimation error in spDNI as a function of AOD x SSA for four aerosol types. Seven AODs are used for each aerosol type, such as 0.01, 0.05, 0.1, 0.2, 0.5, 1.0 and 1.5. The error bars are due to the daily variation for the effective time domain.

775

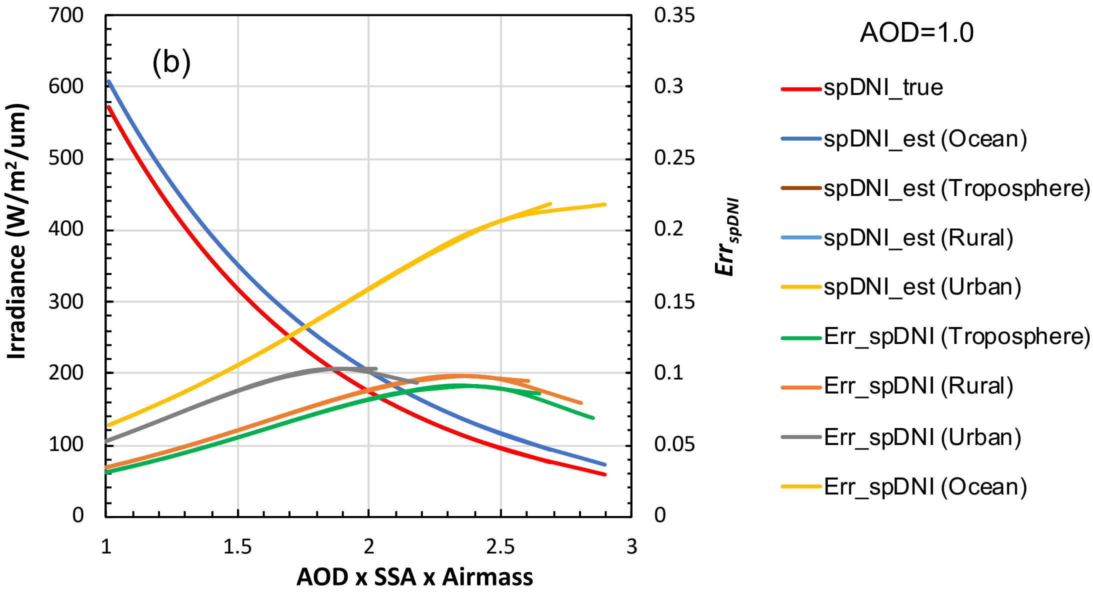

Fig. 8b Examples of spDNI and Err_{spDNI} as a function of AOD x SSA x Airmass for four aerosol types with AOD of 1.0. The estimated spDNIs (spDNI_est) for each aerosol type overlap on the same lines due to small differences. The patterns of Err_{spDNI} show peaks depending on the aerosol type.

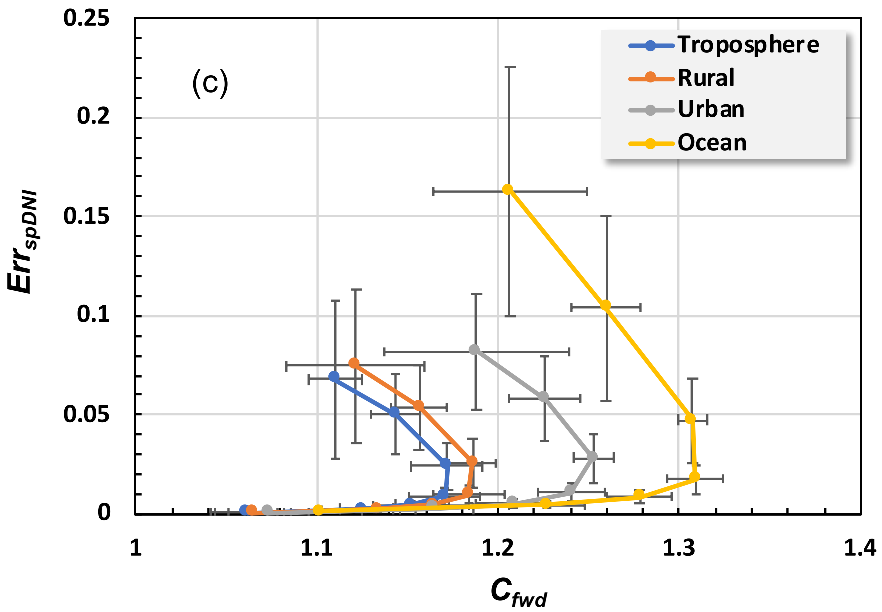

Fig. 8c Relative error in spDNI as a function of C_{fwd}. Seven AODs are used as the same in Fig.8a for each aerosol type. The upper ends of each line are for AOD=1.5. The error bars are the same as in Fig.8a.

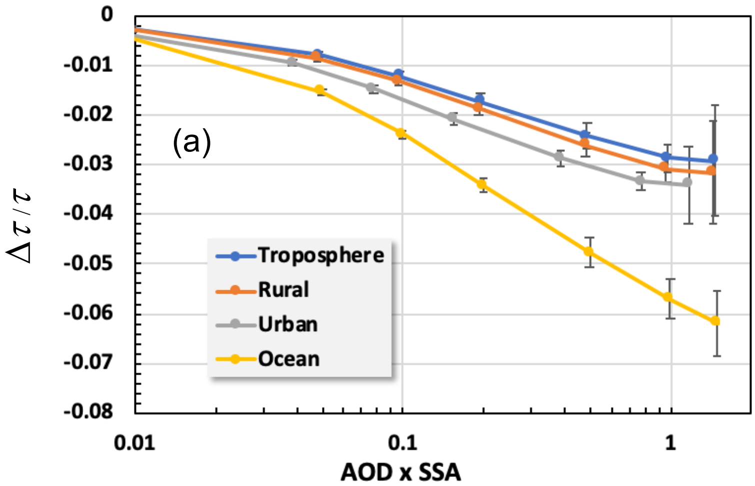

Fig. 9a Relative error in optical depth as a function of AOD x SSA. The four lines with error bars indicate different aerosol types for seven AODs, 0.01, 0.05, 0.1, 0.2, 0.5, 1.0 and 1.5. The rightmost ends of each line are for AOD=1.5.

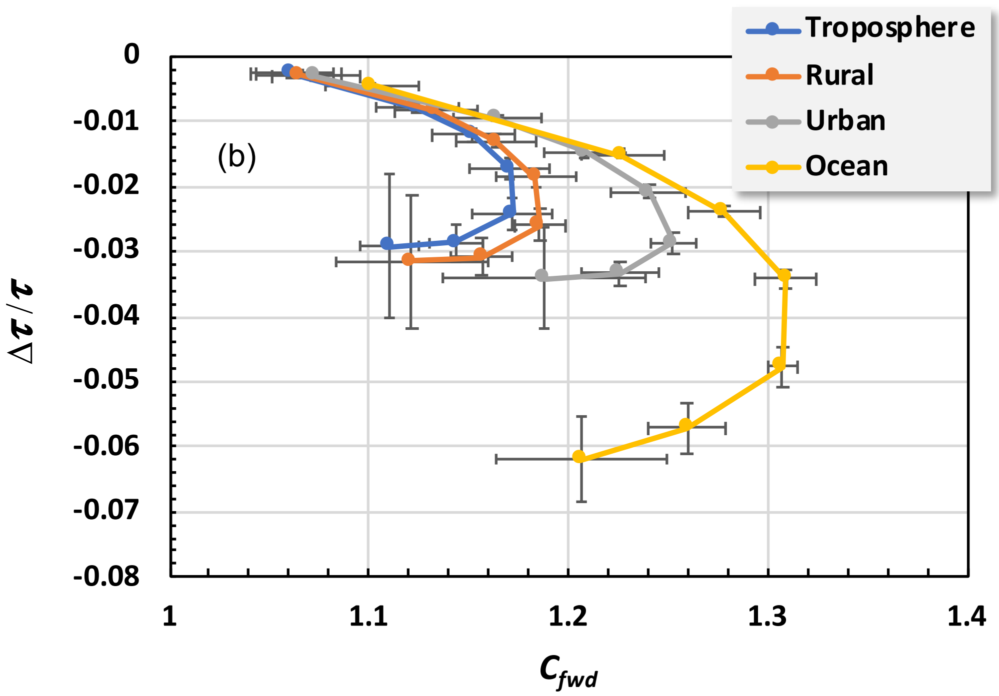

Fig. 9b Estimation error in optical depth as a function of C_{fwd}. The four lines with error bars indicate different aerosol types for seven AODs, 0.01, 0.05, 0.1, 0.2, 0.5, 1.0 and 1.5. The lowest ends of each line are for AOD=1.5, and the smallest (upper) points are for AOD=0.01.

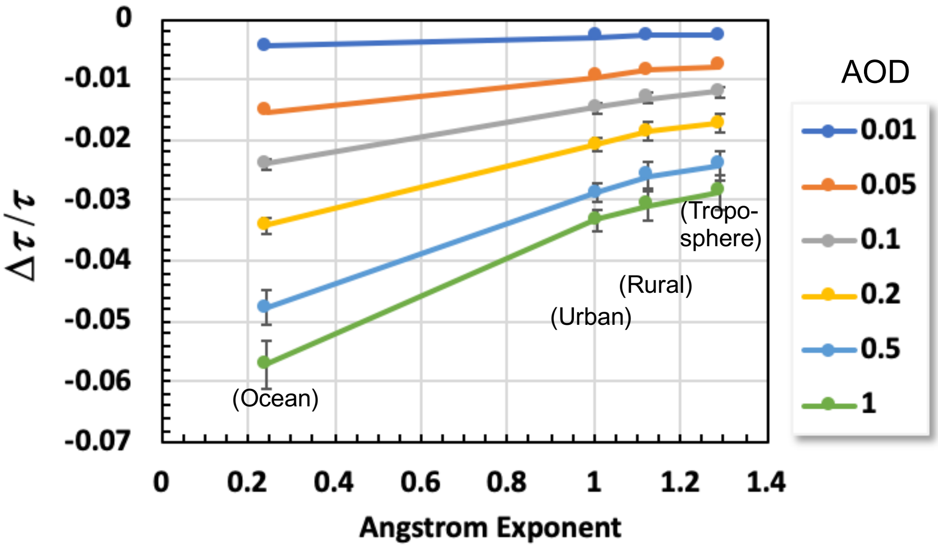

Fig. 10 Relation between $\Delta\tau/\tau$ and Angstrom Exponent.

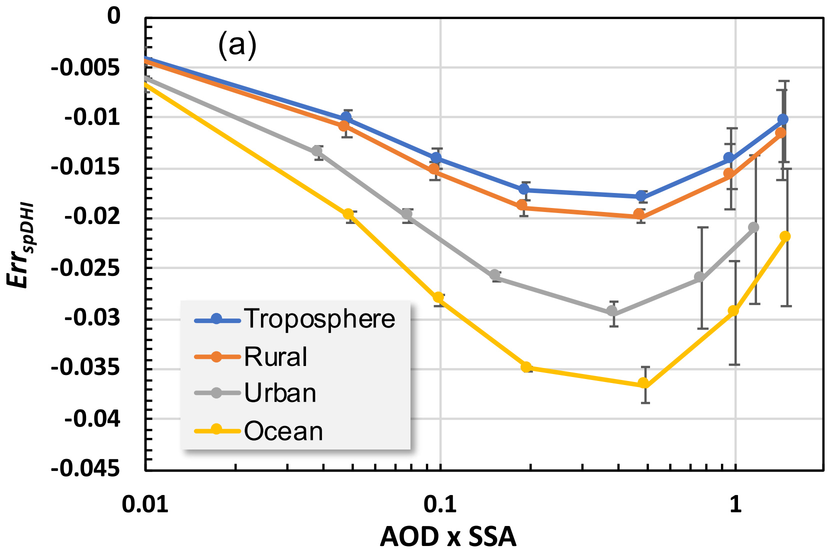

Fig. 11a Relative error in spDHI estimation as a function of AOD x SSA. Each aerosol type shows the minimum points during a range of 0.1 to 1.0 AOD x SSA.

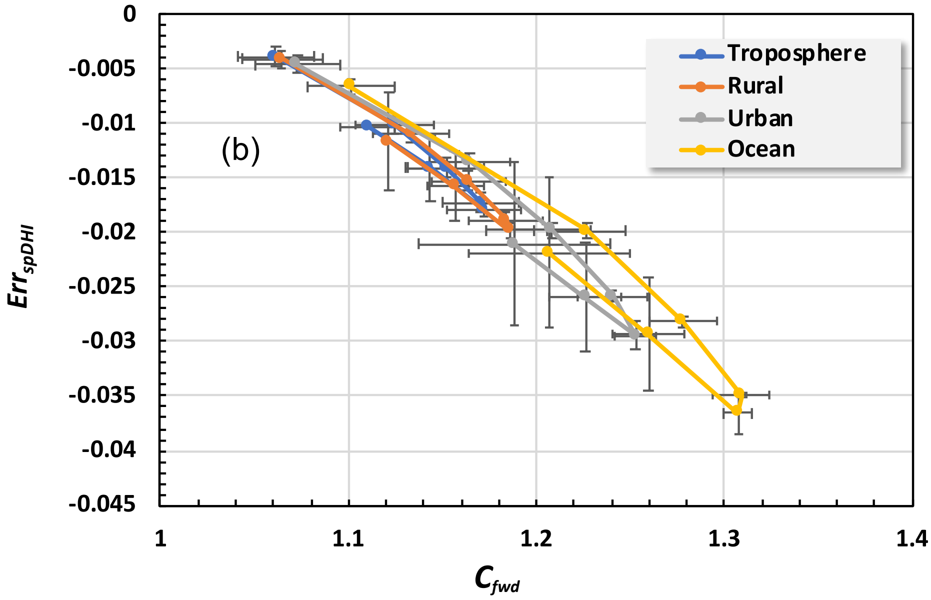

Fig. 11b Same as Fig. 11a except for as a function of C_{fwd}. The minimum point of the error for the Oceanic aerosol type corresponds to the maximum C_{fwd}.

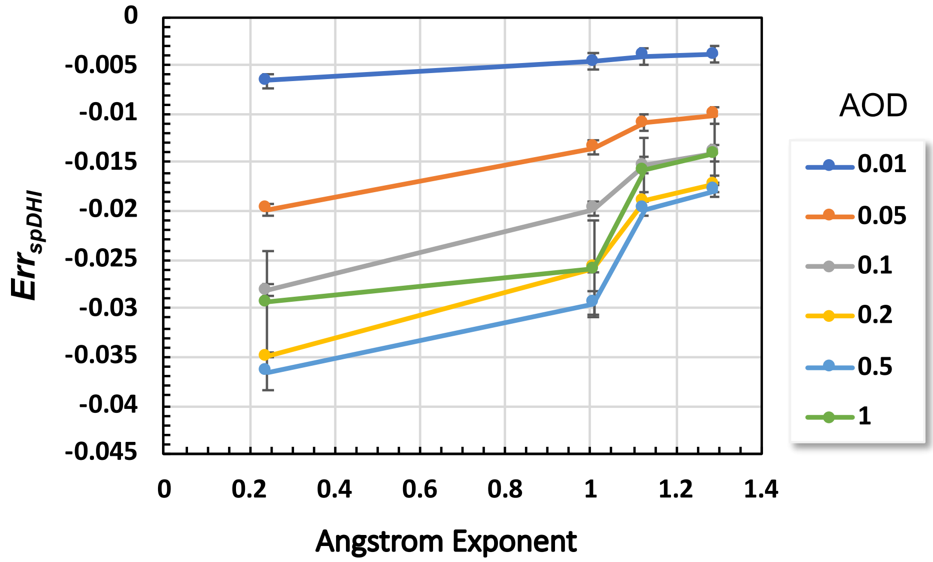

Fig. 12 Relative error in spDHI estimation as a function of the Angstrom Exponent (AE) with different AODs, ranging from 0.01 to 1.0. Four aerosol types are shown corresponding to their AEs.

List of Tables

Table 1a MS-700 specifications

Specification	Value	unit	Remark
Spectral range	350 - 1050	nm	
Readable interval	3.3	nm	
Resolution	10	nm	
Spectral accuracy	Less than 0.3	nm	
Stray light suppression	0.15	%	
Angular dependency of diffuser/sensor	7	%	Incident angle between 0 and 80 deg.
Temperature dependency	±1.0	%	Temperature range of -20 to 50 deg.
Temperature control	25 ± 5	deg.	
Operation temperature	-10 to +40	deg.	

Table 1b MB-22 specifications

Specification	Value	unit	Remark
Rotating radius	200	mm	Radius of the rotating band
Band width/Thickness	30/4	mm	
Shadowing angle	8.6	deg	
Overhung angle	35.0	deg	Angle from the zenith
Slant angle of rotating axis	15.0	deg	Angle from the horizon
Initial position of band	150.0	deg	Zenith angle
Angle for irradiance compensation	±10.0	deg	Deviation angles from the angle at which band completely shadows the direct solar irradiance

Table 2 Model and parameters for simulation

Specification	Type/Value	Remark
Atmospheric model	Mid-Latitude Summer	Pressure: 1013.25hPa
Precipitable water content	30.0 mm	
Ozone amount	300.0 DU	
Surface albedo	0.15	500 nm
Aerosol	Rural/Urban Ocean/Troposphere	AOD (500 nm): 0.001, 0.005, 0.01, 0.02, 0.05, 0.1, 0.2, 0.5, 1.0, 1.5, 2.0
Solar spectrum	MODTRAN_3	Built-in SBDART
Location	Lat.=35.624, Lon.=140.104	SKYNET Chiba Univ.
Date	June 22, 2016	Sun-Earth distance: 1.0 AU fixed

Table 3 Single scattering albedo and asymmetry factor at 500 nm and Angstrom exponent used in the simulation.

	Troposphere	Rural	Urban	Ocean
Single Scattering Albedo	0.973	0.959	0.774	0.993
Asymmetry Factor	0.689	0.700	0.737	0.768
Angstrom Exponent	1.291	1.126	1.006	0.243

Table 4 Summary of mean correction coefficient and relative error in spDNI, spDHI and optical depth estimation. Each value is a daily mean with the standard deviation for two AODs.

	AOD	Troposphere	Rural	Urban	Ocean
C_{fwd}	0.5	1.172 ± 0.013	1.186 ± 0.013	1.253 ± 0.011	1.307 ± 0.008
	1.0	1.144 ± 0.015	1.157 ± 0.015	1.226 ± 0.019	1.260 ± 0.019
Err_{spDNI} (%)	0.5	2.4 ± 1.2	2.6 ± 1.2	2.8 ± 1.2	4.7 ± 2.1
	1.0	5.0 ± 2.0	5.4 ± 2.2	5.8 ± 2.1	10.4 ± 4.5
Err_{spDHI} (%)	0.5	-1.8 ± 0.1	-2.0 ± 0.1	-2.9 ± 0.1	-3.7 ± 0.2
	1.0	-1.4 ± 0.3	-1.6 ± 0.3	-2.6 ± 0.5	-2.9 ± 0.5
$\Delta\tau/\tau$ (%)	0.5	-2.4 ± 0.2	-2.6 ± 0.2	-2.9 ± 0.2	-4.8 ± 0.3
	1.0	-2.9 ± 0.3	-3.1 ± 0.3	-3.3 ± 0.2	-5.7 ± 0.4